# X. PLASMA ELECTRONICS*


| | | |
|---|---|---|
| Prof. L. D. Smullin | W. L. Brassert | S. Puri |
| Prof. H. A. Haus | R. J. Briggs | W. D. Rummler |
| Prof. A. Bers | S. A. Evans | A. J. Schneider |
| Prof. G. Fiocco | E. T. Gerry | P. E. Serafim |
| Prof. W. D. Getty | B. A. Hartenbaum | P. S. Spangler |
| Prof. D. J. Rose | H. Y. Hsieh | G. Theodoridis |
| Prof. T. H. Dupree | G. I. Kachen | E. Thompson |
| Prof. L. M. Lidsky | L. N. Lontai | P. B. Ulrich |
| Prof. E. P. Gyftopoulos | D. L. Morse | C. E. Wagner |
| F. Alvarez de Toledo | R. T. Nowak | H. L. Witting |
| R. R. Bartsch | L. M. Petrie, Jr. | J. C. Woo |


## A. BEAM-PLASMA DISCHARGES

### 1. SYSTEM A

In this report we give a more detailed interpretation of the magnetic probe observations,[1] and some experimental observations of VHF oscillations in the beam-plasma discharge which are believed to be ion-plasma oscillations.

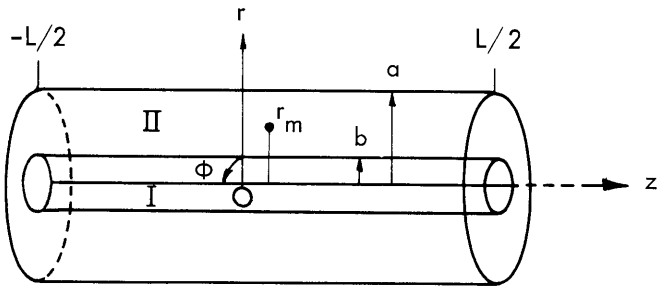


REGION I Defined by the luminous beam-plasma discharge; b is typically 1/2 inch

REGION II The magnetic probe is located here ($r = r_m$); it extends from the edge of the luminous discharge to the metallic cavity wall ($r = a = 2$ inches)

Fig. X-1. Theoretical model for magnetic probe calculation.

First, we shall use the following model to interpret the magnetic-probe observations (Fig. X-1).


*This work was supported in part by the National Science Foundation (Grant G-24073); and in part by Purchase Order DDL BB-107 with Lincoln Laboratory, a center for research operated by Massachusetts Institute of Technology with the joint support of the U.S. Army, Navy, and Air Force under Air Force Contract AF 19(604)-7400.

a. Model

(i) We idealize our interaction region into a metallic cavity of radius a short-circuited at the two ends, at which $z = \pm L/2$.

(ii) We assume that a uniform induction $B_o$ is established throughout by the Helmholtz coils located at $z = \pm L/2$.

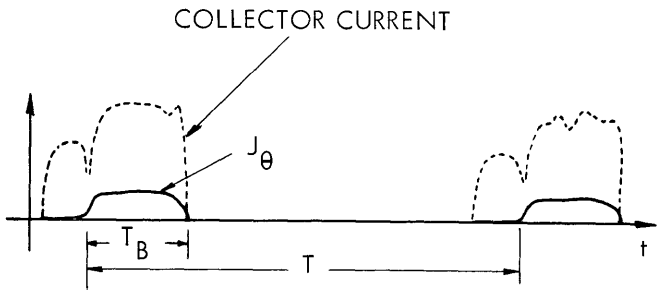


Fig. X-2. Time relationship of surface azimuthal current and collector current.

(iii) We postulate that a surface azimuthal current exists at r = b which accounts for the diamagnetic effect. The current is specified by the time and space behavior shown in Fig. X-2, and given by

$$\vec{J} = -\vec{i}_\theta \frac{I_o \pi}{2L} \cos\frac{\pi z}{L} \delta(r-b) \sum_{n=0}^{\infty} [u_{-1}(t-nT) - u_{-1}(t-T_b-nT)] \tag{1}$$

The z cosine is convenient for cavity solutions.

(iv) We neglect the inertia force in the equation of motion, and for the pressure P we obtain

$$\nabla P = \vec{J} \times \vec{B}. \tag{2}$$

(v) We assume that $\partial/\partial\theta = 0$ and $J_r = J_z = 0$; then

$$\frac{\partial}{\partial r} P = J_\theta B_z,$$

so that

$$\frac{I_o \pi}{2L} = \frac{n_o e T_-}{B_o}. \tag{3}$$

b. Calculations

An exact solution of the problem still has not been carried out. The simplest model that seems to be logical is one in which the current $J_\theta$ is confined to the surface r = b

and it is assumed that $\epsilon = \epsilon_o$ in both regions I and II. (A more realistic model is being studied.)

The beam-plasma discharge has been replaced, in this calculation, by a surface current at r = b. The low frequencies of interest allow us to use "magneto quasi statics" to calculate the spatial dependence of H from Laplace's equation. In particular, we are interested in the least radial variation of the circularly symmetric field. The magnetic fields of interest are

$$\overline{H_I} = -\frac{\pi}{L} C_1 I_o\left(\frac{\pi r}{L}\right) \cos \frac{\pi z}{L} \vec{i}_z - \frac{\pi}{L} C_1 I_1\left(\frac{\pi r}{L}\right) \sin \frac{\pi z}{L} \bar{i}_r$$

$$\overline{H_{II}} = -\frac{\pi}{L} \cos \frac{\pi z}{L} \left\{C_2 I_o\left(\frac{\pi r}{L}\right) + C_3 K_o\left(\frac{\pi r}{L}\right)\right\} \vec{i}_z$$

$$-\frac{\pi}{L} \sin \frac{\pi z}{L} \left\{C_2 I_1\left(\frac{\pi r}{L}\right) - C_3 K_1\left(\frac{\pi r}{L}\right)\right\} \bar{i}_r$$

The three boundary conditions that permit us to determine the three constants $C_1$, $C_2$, $C_3$ are:

(i) continuity of the radial magnetic field at r = b;

(ii) the vanishing of the radial magnetic field at r = a; and

(iii) the difference of the z component of the magnetic field at r = b is equal to the surface current.

Using the small-argument expansion for the Bessel functions, we obtain for the z component of the magnetic field

$$B_I = \mu_o \frac{\pi I_o}{2L} \frac{1 - \frac{a^2}{b^2}}{\frac{a^2}{b^2} + \frac{1}{2}\left(\frac{\pi a}{L}\right)^2 \log \frac{L}{\pi b}} \cos \frac{\pi z}{L}$$

$$B_{II} = \mu_o \frac{\pi I_o}{2L} \frac{1 + \frac{1}{2}\left(\frac{\pi a}{L}\right)^2 \log \frac{L}{\pi r_m}}{\frac{a^2}{b^2} + \frac{1}{2}\left(\frac{\pi a}{L}\right)^2 \log \frac{L}{\pi b}} \cos \frac{\pi z}{L} \qquad \text{at } r = r_m.$$

In the experiments we measure $B_{II}$. In Quarterly Progress Report No. 70 (pages 107-111), we inferred an electron temperature from

$$T_- = \frac{B_o}{\mu_o} \frac{B_{II}}{n_o e} = 11 \text{ ev.} \tag{4}$$

Now it is shown that at z = 0

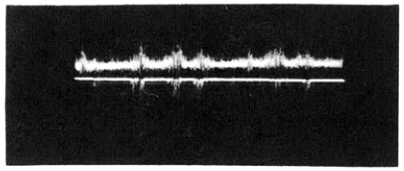


Fig. X-3. Oscillogram of groups of kmc oscillations (horn) and groups of VHF oscillations (140 mc).

P = 0.7 μ Hg $B_o$ = 660 gauss
$V_b$ = 5 kv $I_{coll}$ = 0.26 amp
Time, 20 μsec/cm Hydrogen

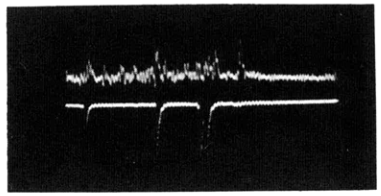


Fig. X-4. Oscillogram of spikes of kmc oscillations (horn) and spikes of VHF oscillations (160 mc).

P = 0.67 μ Hg $B_o$ = 660 gauss
$V_b$ = 5 kv $I_{coll}$ = 0.32 amp
Time, 2 μsec/cm Hydrogen

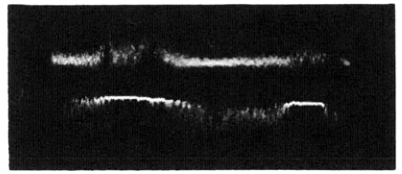


Fig. X-5. Oscillogram of groups of oscillations at lower magnetic fields.

P = 0.7 μ Hg $B_o$ = 440 gauss
$V_b$ = 5 kv $I_{coll}$ = 0.26 amp
Time, 20 μsec/cm Hydrogen

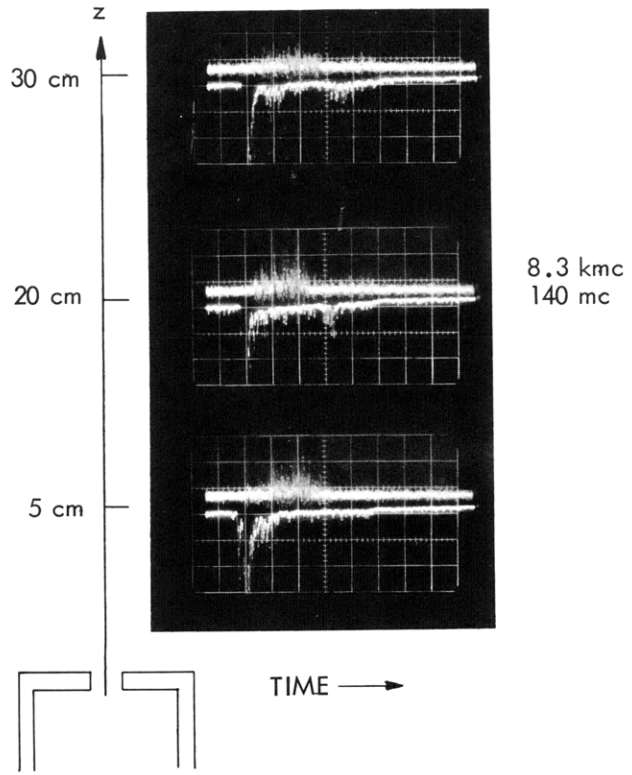


Fig. X-6. Oscillograms showing oscillation amplitude dependence as a function of axial position. The 140-mc oscillation is picked up by a loop. The 8.3-kmc oscillation is picked up by a fixed loop. The movable loop was at the axial positions indicated for the three pictures. The vertical calibrations are the same in all oscillograms.

P = 0.35 μ Hg $B_o$ = 330 gauss
$V_b$ = 5 kv $I_{coll}$ = 0.28 amp
Time, 20 μsec/cm Hydrogen

$$T_- = \frac{B_o}{\mu_o}\frac{B_{II}}{ne}\frac{\frac{a^2}{b^2}+\frac{1}{2}\left(\frac{\pi a}{L}\right)^2 \log\frac{L}{\pi b}}{1+\frac{1}{2}\left(\frac{\pi a}{L}\right)^2 \log\frac{L}{\pi r_m}},$$

which for Eq. 4 yields

$$T_- = 14.3(11) = 157 \text{ ev.}$$

We observed some VHF oscillations that we believe to be plasma-ion oscillations. All of the experiments reported on here were performed in hydrogen gas. The following observations were made.

(i) In any given set of conditions leading to a beam-plasma discharge, it is possible to detect VHF (few hundred megacycle) and kmc (4-15 kmc) oscillations that are related by factors in the range 43-61 (the square root of the ion-electron mass ratios of $H^+$ and $H_2^+$).

(ii) Using a broadband "video" detector for the kmc signals (x-band horn-crystal-video amplifier) and a spectrum analyzer for the VHF oscillations (10-mc bandwidth) (with appropriate filters, pads, and line stretcher tuners), we observed the following time structure of the oscillations.

(a) At high magnetic fields (660 gauss) the VHF oscillations and kmc oscillations appear as groups of spikes. These groups occur synchronously in time (Fig. X-3). Within each group, it appears that the large-amplitude kmc and VHF spikes are anti-coincident (Figs. X-3 and X-4).

(b) When the spikes do appear to occur synchronously, the amplitudes of both are small.

(c) At lower magnetic fields (440 gauss), when groups of spikes occur, the VHF groups occur alternately with groups of kmc oscillation (Fig. X-5).

(iii) The VHF oscillations during the beam-plasma discharge show a definite amplitude dependence as a function of position (Fig. X-6). The initial large pulse appears to be larger near the gun than it is near the collector. The oscillations that occur later have the opposite variation (larger near the collector).

H. Y. Hsieh

References

1. H.Y. Hsieh, Beam-plasma discharges, System A: Magnetic probe, Quarterly Progress Report No. 70, Research Laboratory of Electronics, M.I.T., July 15, 1963, pp. 107-111.

## 2. SYSTEM C

We have had a little more operating experience with this new system. (See Quarterly Progress Report No. 70, pages 114-116, for a description.) The important new observation

is that with gas pressures in the range $3\text{-}6 \times 10^{-5}$ mm Hg of hydrogen, the x-ray intensity and energy are very great. The energy is great enough to be detectable through 0.125 inch of lead (or 1.125 inches of aluminum), and there is significant x radiation as long as $5 \times 10^{-3}$ sec after the pulse is over. These observations were made with a field of approximately 2000 gauss and a 7-kv, 8-10 amp beam pulse.

L. D. Smullin

## B. ROTATING PLASMA INSTABILITIES

### 1. Introduction

It is known that a plasma may be unstable against perturbations that tend to drive it across its confining magnetic field. These instabilities have been studied to determine the conditions under which they may exist and be controlled.

### 2. Equations and Assumptions

The conservation of momentum is written in the form of the electron and ion flow equations in Cartesian coordinates, with the magnetic field in the +z direction. End walls are placed at $z = \pm L/2$.

$$\Gamma_{\pm\perp} = \overline{\overline{D}}_{\pm} \cdot \overline{\nabla} n_{\pm} \mp n_{\pm} \overline{\overline{\mu}}_{\pm} \cdot \overline{\nabla} V$$

$$\Gamma_{\pm z} = n_{\pm} \overrightarrow{V}_{iT} \left(\frac{z}{L}\right); \qquad \frac{\partial n_{\pm}}{\partial z} = 0 \quad \frac{\partial V}{\partial z} = 0. \tag{1}$$

In the tensors $\overline{\overline{D}}$ and $\overline{\overline{\mu}}$ the diagonal elements are the perpendicular terms, and the off-diagonal elements are the Hall terms. Frequencies of interest lie far below the ion-plasma frequency; inertia terms are omitted and wave-propagation phenomena are not considered. The longitudinal equations are given the simple form because it is assumed that a mean-free path is long compared with the container length. The longitudinal electron and ion currents are equalized by ion sheaths at the end walls, as is often the case in practice.

To complete the set of equations, we need the continuity equations for electrons and ions and Poisson's equation.

$$\frac{\partial n_{\pm}}{\partial t} + \overline{\nabla} \cdot \overline{\Gamma}_{\pm} = 0 \tag{2}$$

$$\nabla^2 V = -\frac{e}{\epsilon_o}(n_+ - n_-). \tag{3}$$

We reduce this set of equations to a pair of coupled scalar differential equations by making the neutrality assumption ($n_- = n$, $n_+ = n+\delta$, $|\delta| \ll n$) and linearizing for small

perturbations of density and potential about time-invariant values.

$$n_{\pm}(x, y, t) = n_o(x) + n'(x)\, e^{j\omega t+iky}$$
$$V(x, y, t) = V_o(x) + V'(x)\, e^{j\omega t+iky}. \tag{4}$$

The resulting equations may be written

$$O_A n' + O_B V' = 0$$
$$O_C n' + O_D V' = 0, \tag{5}$$

where the O's are linear second-order differential operators.

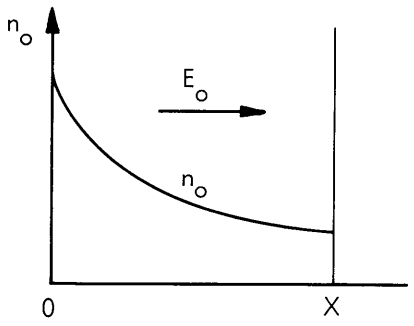


Fig. X-7. Unperturbed density and electric field.

If the zero-order solutions have the form (see Fig. X-7)

$$n_o(x) = n_o\, e^{-x/x_o}$$
$$V_o(x) = -E_o x + \phi_o, \qquad E_o \gtrless 0 \tag{6}$$

then the coupled equations (5) may be reduced to a single fourth-order differential equation:

$$(i\omega+a_L)\left(\frac{ik}{x_o}(\mu_{eH}-\mu_{iH})+(\mu_{e\perp}+\mu_{i\perp})O_1\right) n(x) + \frac{ik}{x_o}(\mu_{iH}D_{e\perp}-\mu_{eH}D_{i\perp})\, O_2 n(x)$$
$$- ikE_o(\mu_{iH}\mu_{e\perp}+\mu_{eH}\mu_{i\perp})\, O_2 n(x) - (\mu_{e\perp}D_{i\perp}+\mu_{i\perp}D_{e\perp})\, O_1 O_2 n(x) = 0. \tag{7}$$

We have made the following definitions in Eq. 7:

$$a_L = \frac{\overline{V_{iT}}}{L}$$
$$n(x) = n'(x)\, e^{x/x_o}$$

$$O_1(x) = \frac{\partial^2}{\partial x^2} - k^2 - \frac{1}{x_o}\frac{\partial}{\partial x}$$

$$O_2(x) = \frac{\partial^2}{\partial x^2} - k^2 - \frac{2}{x_o}\frac{\partial}{\partial x} + \frac{1}{x_o^2}.$$

To solve Eq. 7, we shall neglect the last term [which contains the third and fourth derivatives of n(x)] and solve the remaining second-order differential equation subject to the boundary conditions

$$n(0) = 0$$
$$n(X) = 0. \qquad (8)$$

For each eigenfunction n(x) we find a complex eigenvalue $\omega$. Finally, the last term in (7) is introduced as a perturbation.

3. Results

Equation 7 is solved under the assumptions that

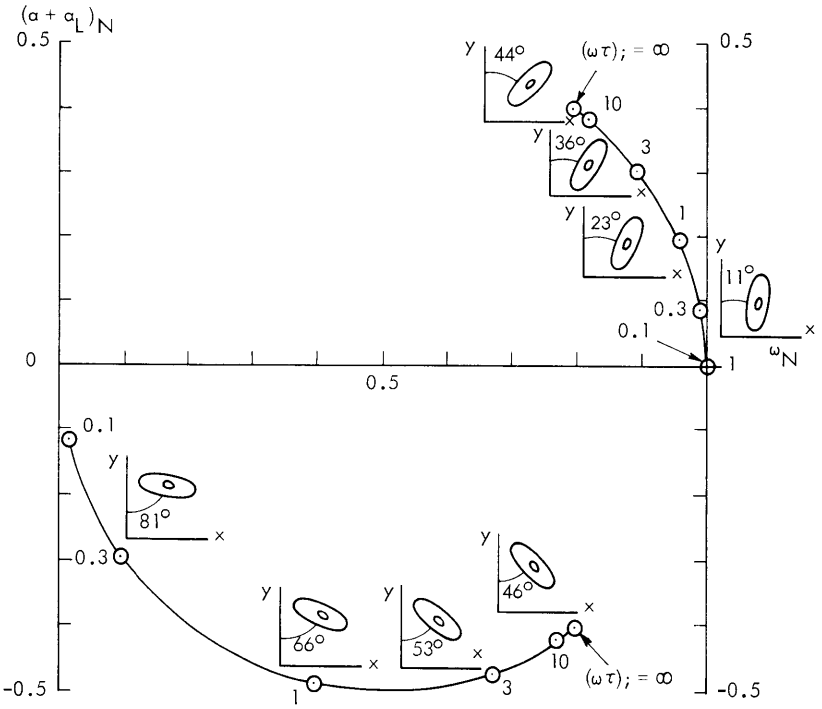


Fig. X-8. Normalized eigenvalues and eigenfunctions with $\omega_{ci}\tau_i$ a parameter. Eigenfunctions n'(x) shown as contour maps in the x-y plane. Size parameters: $kx_o = 1$ $\pi x_o/X = 1/4$.

$$\omega_{ce}\tau_e \gg 1 \text{ and } \frac{\omega_{ci}\tau_i}{\omega_{ce}\tau_e} \ll 1,$$

with $\omega_{ci}\tau_i$ a parameter. The eigenvalues $\omega$ and contour maps of the eigenfunctions $n'(x) = n(x)\, e^{-x/x_o}$ are shown in Fig. X-8. The eigenvalues are normalized to $kE_c/B$, where $E_c$ is a "corrected" electric field,

$$E_c = E_o - \frac{1}{x_o}\left(\frac{\omega_{ci}\tau_i}{\omega_{ce}\tau_e} T_e - T_i\right). \tag{9}$$

Since $0 < \omega_N < 1$, the perturbation moves with a velocity less than $E_c/B$, a corrected Hall velocity. The upper branch of Fig. X-8 represents growing perturbations for $E_c > 0$, and the lower branch for $E_c < 0$.

4. Instability Mechanisms

To investigate the instability mechanisms, we must examine the shape of the perturbed density eigenfunctions. These eigenfunctions are shown as contour maps in the x-y plane. The smallest loop indicates the perturbed density peak, and the larger loops are contours of constant (perturbed) density.

Let us consider the case $\omega_{ci}\tau_i \gg 1$. In this case, the Hall mobilities for electrons and ions are equal. The eigenfunction for $E_c > 0$ is shown in Fig. X-9. With $E_o > 0$ or with $(\omega_{ci}\tau_i/\omega_{ce}\tau_e)\, T_e - T_i < 0$ $(D_{i\perp} > D_{e\perp})$, a charge separation is established. The resulting E field has a component in the +y direction which will drive the particles outward because of the Hall mobility.

When $E_c < 0$, the eigenfunction is as shown in Fig. X-10. Now with $E_o < 0$ or $(\omega_{ci}\tau_i/\omega_{ce}\tau_e)\, T_e - T_i > 0$ $(D_{e\perp} > D_{i\perp})$, the indicated charge separation is achieved, and once more an electric field in the +y direction is obtained to drive the instability.

As $\omega_{ci}\tau_i$ is decreased, there begins to be an appreciable difference between the electron and ion Hall mobilities. As a result, new mechanisms appear. For $E_c < 0$, $\omega_{ci}\tau_i = 1$, the eigenfunction is as shown in Fig. X-11. For $E_o < 0$, the charge separation shown is mainly due to the difference in Hall mobilities. When $(\omega_{ci}\tau_i/\omega_{ce}\tau_e)\, T_e - T_i > 0$, diffusion effects create the separation indicated. This is similar to the case worked out by Simon[1] who used a "trial function" similar to the eigenfunction in Fig. X-11.

When $E_c > 0$ at $\omega_{ci}\tau_i = 1$, the eigenfunction appears as in Fig. X-12. When $E_o > 0$, the perturbations must slant steeply to allow the charge separations resulting from the perpendicular mobility to overcome that which is due to the Hall mobility. Similarly, where $(\omega_{ci}\tau_i/\omega_{ce}\tau_e)\, T_e - T_i < 0$, diffusion creates the separation shown.

Hall diffusion does not enter into these arguments, since the particle currents caused by Hall diffusion are divergence-free. Note that the Hall diffusion coefficients do not appear in (9).

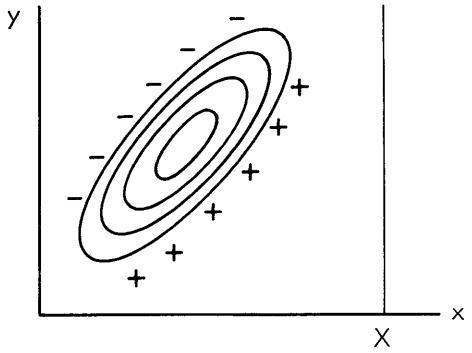


Fig. X-9. Eigenfunction for $\omega_{ci}\tau_i \gg 1$, $E_c > 0$.

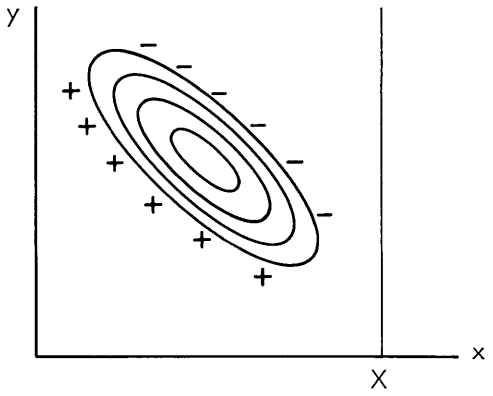


Fig. X-10. Eigenfunction for $\omega_{ci}\tau_i \gg 1$, $E_c < 0$.

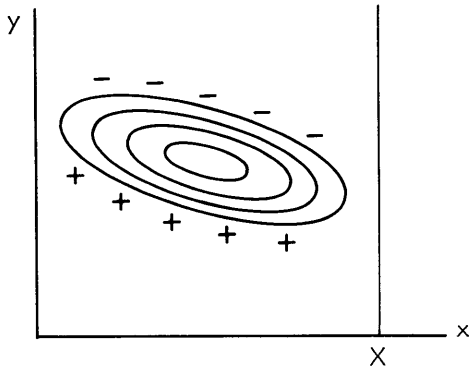


Fig. X-11. Eigenfunction for $\omega_{ci}\tau_i = 1$, $E_c < 0$.

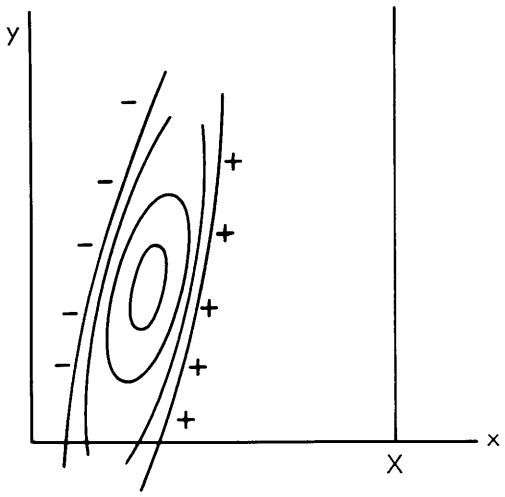


Fig. X-12. Eigenfunction for $\omega_{ci}\tau_i = 1$, $E_c > 0$.

5. Stabilizing (Loss) Mechanisms

To evaluate the effect of parallel loss, it is helpful to unnormalize the eigenvalue plot. This is done in Fig. X-13 for two values of $k|E_c|/B$. The gain constant $\alpha$ for growing perturbations is the vertical distance between the curve and the shaded area.

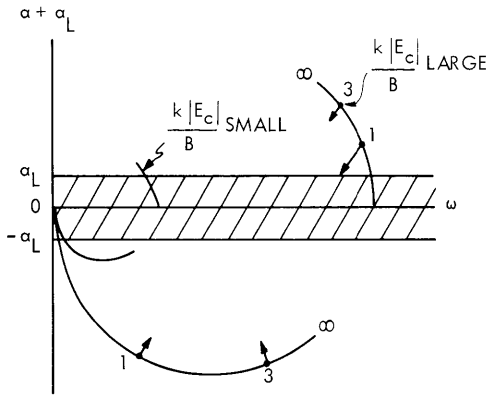


Fig. X-13. Unnormalized eigenvalue plot.

Finally, we introduce the perpendicular loss as a perturbation of our results. The shift in eigenvalue is indicated in the "$k|E_c|/B$ large" plot by the inward-pointing arrows. The greatest damping effect occurs on the $E_c > 0$ branch, where the eigenfunctions tilt sharply (see Fig. X-12).

In general, sufficiently large B will drive the eigenvalues into the parallel-loss region. Low values of B decrease $\omega_{ci}\tau_i$ and increase the perpendicular loss until the gain is swamped out.

6. Correlation between Theory and Experiment[2,3]

Figure X-14 is a plot of measured and calculated rotational period against magnetic field. The rotational period decreases for increasing B because the measured radial electric field increases with B. Curve (a) shows the measured period, and (b) is the period calculated from the measured value of $E_o/B$, 2 inches from the axis. $E_o$ varies from 12 v/m to 44 v/m, from the left to the right ends of the curve. Curve (c) is the period calculated from $0.9\,E_c/B$ by using $x_o = 1$ cm and $T_i = 0.1$ volt.

Perpendicular loss is important for $\omega_{ci}\tau_i < 3$ and $E_c > 0$ (our case). It becomes rapidly more important as k is increased. This would indicate that in cylindrical geometry modes above m = 1 would be highly damped. In our experiment, we see only one spoke (m=1).

At $\omega_{ci}\tau_i = 3$, we calculate that we would need $E_c = 20$ v/m to overcome the stabilizing effects. This is approximately the value of $E_c$ at which the instability is observed to

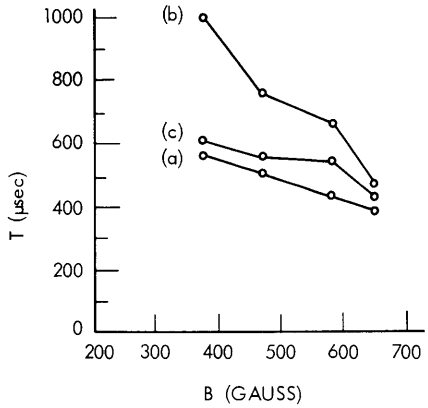


Fig. X-14. Comparison between measured and calculated rotational period.

appear. But $E_c$ increases faster than B over the range of magnetic field available, so that we are unable to quench the instability.

D. L. Morse

References

1. A. Simon, Instability of a partially-ionized plasma in crossed electric and magnetic fields, Phys. Fluids 6, 382 (1963).

2. D. L. Morse, Instability in the hollow-cathode discharge, Quarterly Progress Report No. 69, Research Laboratory of Electronics, M.I.T., April 15, 1963, p. 54.

3. D. L. Morse, Instability in the hollow-cathode discharge, Quarterly Progress Report No. 70, Research Laboratory of Electronics, M.I.T., July 15, 1963, pp. 117-121.

## C. CRITERIA FOR DETERMINING ABSOLUTE INSTABILITIES AND DISTINGUISHING BETWEEN AMPLIFYING AND EVANESCENT WAVES

We have established mathematical criteria and procedures that enable one to determine and distinguish absolute (nonconvective) instabilities, amplifying waves (convective instabilities), evanescent (decaying) waves,and the direction of signal flow in propagating waves. These criteria are free from the difficulties and limitations of previous attempts.[1-6] Here, we shall give a brief outline of the proof of these criteria and show the physical interpretation that is associated with them.

### 1. Problem

Consider a general system that is uniform in time (time-invariant) and uniform in (at least) one spatial dimension, say z. Perturbations of such a system, described by linearized equations, are of the form $f(\bar{r}_T)$ exp $j(\omega t-kz)$, where $\bar{r}_T$ is the

two-dimensional vector coordinate that is transverse to z. The condition for the existence of such solutions, together with their satisfaction of the boundary conditions transverse to z is expressed in the dispersion relation

$$D(\omega, k) = 0. \tag{1}$$

(Note that if the system is uniform in all spatial coordinates, the perturbations are of the form $\exp j(\omega t - \bar{k} \cdot \bar{r})$ and the dispersion relation that results directly from the linearized equation is $D(\omega, \bar{k}) = 0$.)

Equation 1 is, in general, a relation between the complex frequency, $\omega(\omega = \omega_r + j\omega_i)$, and the complex wave number, $k(k = k_r + jk_i)$. The problem that remains is that of determining the meaning of the various possible solutions to Eq. 1. Thus we would like to know whether the uniform system exhibits any absolute instabilities, and if it does, then what is the growth rate in time of this instability? If it does not, then at a particular steady-state excitation which waves are amplifying, which are evanescent, and in which direction do the purely propagating waves leave the source?

In order to determine the meaning of these solutions to Eq. 1, we shall study systems that are of infinite extent in z. One should bear in mind, however, that the effect of boundaries that limit the extent in z can be crucial in determining the behavior of a given physical system. For example, the presence of reflecting boundaries at some finite z can, in some cases, lead to growth in time even if the system supports only convective instabilities when it is uniform in z.

## 2. Excitation and Response of the System

In order to interpret the various possible solutions to Eq. 1, we consider the problem of excitation of the uniform system. Since we are allowing for possibly unstable systems, it is of utmost importance to introduce conditions of causality in both time and space. (The system is uniform in z, and at $z = \pm\infty$ there are no sources.) Hence we choose a source that is localized in space (say, in the region $|z| < d$) and which is "turned on" at $t = 0$. Let this source function be $S(t, z)$ and let the response of the system to this source function be $\Psi(t, z)$. Hereafter we shall ignore the dependence upon $\bar{r}_T$, since it is not relevant to the criteria that we are seeking. The causality conditions are (a) at any $z\ (|z| > d)$ the response is zero for $t \leq 0$, and (b) at any finite $t\ (t > 0)$ the response will occupy a finite region of space and be zero outside this region. Thus we shall use Laplace transforms in time and Fourier transforms in space and write the response as

$$\Psi(t, z) = \int_L e^{j\omega t} \frac{d\omega}{2\pi} \int_F e^{-jkz} \frac{dk}{2\pi} G(\omega, k) \cdot S(\omega, k), \tag{2}$$

where $G(\omega, k)$ is the Laplace (t)-Fourier (z) transform of the Green's function of the

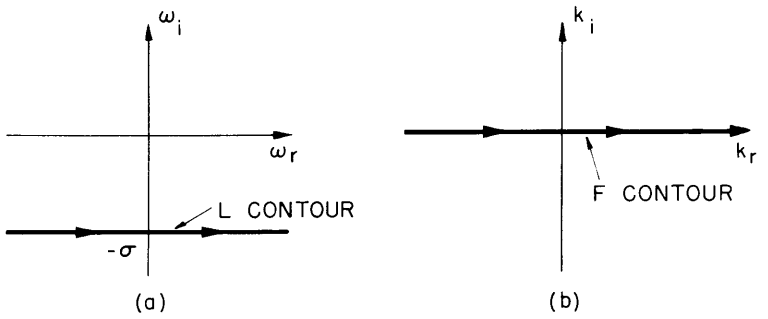


Fig. X-15. Contours pertinent to the integrations in Eq. 2.
(a) Laplace contour L in the complex ω-plane.
(b) Fourier contour F in the complex k-plane.

linearized system equations, and $S(\omega, k)$ is the corresponding transform of the source function $S(t, z)$. The integration over $\omega$ is along the contour L ($-\infty - j\sigma$ to $\infty - j\sigma$), as shown in Fig. X-15a; the contour L must pass below all singularities of the integrand so that the causality requirement is satisfied. The integration over k is along the contour F ($-\infty$ to $+\infty$), the real k axis, as shown in Fig. X-15b. In principle, Eq. 2 contains all of the information that we are seeking. In fact, since it gives the response in detail, it contains more than that in which we are interested, and the detailed evaluation of Eq. 2 is not necessary for our purposes.

3. Waves on the Contour L; the k Integration

The integrations in Eq. 2 can be thought of in the following way. For each complex frequency on the contour L the k integration over the contour F is carried out and yields a function of $\omega$ and z:

$$F(\omega, z) = \int_F G(\omega, k) \cdot S(\omega, k)\, e^{-jkz} \frac{dk}{2\pi}. \tag{3}$$

This function is then integrated over the contour L to give the response

$$\Psi(t, z) = \int_L F(\omega, z)\, e^{j\omega t} \frac{d\omega}{2\pi}. \tag{4}$$

The simplest source function that meets our requirements is the delta-function in both t and z for which $S(\omega, k)$ is unity. This is also sufficient, since our arbitrary source function can be built up by superposition of delta-functions. In any case, since the source function is limited in space, $|z| < d$, it has a transform that is an entire function of k. The Green's function contains all of the natural responses (normal modes) of the system, and these are exhibited by the singularities of $G(\omega, k)$. With the delta-function source, the contour L must be chosen to lie below the lowest singularity of

$G(\omega, k)$ for any real k. Hence $\sigma$ (Fig. X-15a) must be greater than the maximum time-growth rate of any possible natural response (maximum negative $\omega_i$ for real k in Eq. 1).

The singularities of $G(\omega, k)$ are, in general, poles and branch points. In the case of branch points the integrations in Eq. 2 depend strongly upon the type of branch points and branch lines, of which there can be a great variety, and each case must be treated individually. Note that these branch lines of $G(\omega, k)$ will contribute to the response in a source-free region, that is, physically they can be considered to be a "continuum of normal modes." In order to present a general closed-form resolution to our problem, we shall assume that the singularities of $G(\omega, k)$ are only poles. These are then determined by Eq. 1, that is, $G(\omega, k) \sim [D(\omega, k)]^{-1}$. For a particular frequency $\omega_L$ on the

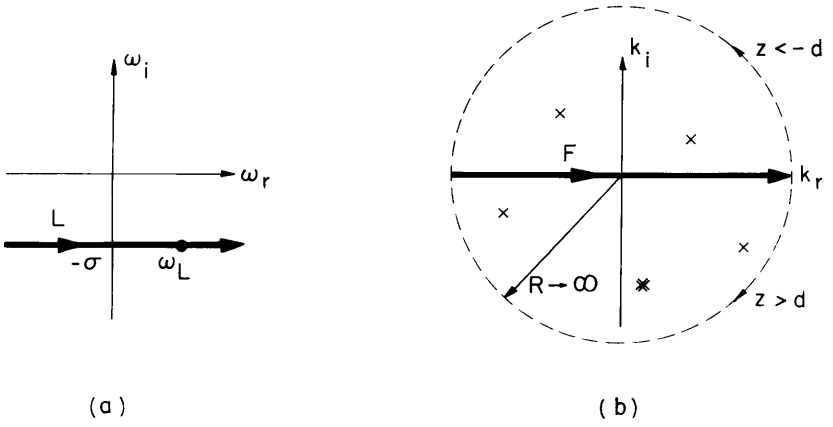


Fig. X-16. For a frequency $\omega_L$ on the contour L (a), the singularities of $G(\omega_L, k)$ in the k-plane are shown in (b).

contour L, the singularities of $G(\omega_L, k)$ in the k-plane are determined from Eq. 1 for $\omega = \omega_L$ and may be as shown in Fig. X-16. Since $S(\omega_L, k)$ is regular in the entire k-plane, these are also the singularities of the integrand of Eq. 3 in the finite k-plane. If the integrand in Eq. 3 is well behaved for large values of $k_i$, as is the case in most physical situations, then the contour F may be closed below the $k_r$ axis for $z > d$ and above the $k_r$ axis for $z < -d$, as shown in Fig. X-16. The integral in Eq. 3 can then be evaluated by Cauchy's residue theorem, and thus we can express $F(\omega_L, z)$ as a sum over the normal modes, that is,

$$F(\omega_L, z > d) = \sum_{\substack{\text{lower half} \\ \text{k-plane} \\ \text{poles}}} j \operatorname{Res}\left[ G(\omega_L, k) S(\omega_L, k)\, e^{-jkz} \right] \tag{5}$$

$$F(\omega_L, z<-d) = \sum_{\substack{\text{upper half} \\ \text{k-plane} \\ \text{poles}}} j\,\text{Res}\left[G(\omega_L, k)S(\omega_L, k)\,e^{-jkz}\right] \tag{6}$$

If $G(\omega_L, k)$ also has branch points, Eqs. 5 and 6 will also have contributions from the contour integrations around the corresponding branch lines in the k-plane.

Hence, by choosing the frequency on the contour L, we are able to determine unequivocally which of the complex k solutions to Eq. 1 will appear for $z > d$ and which will appear for $z < -d$. Note that for $\omega = \omega_L$ the space dependence for all solutions appears evanescent (decaying) in space.

4. Absolute Instabilities

In order to determine whether or not the system exhibits absolute (nonconvective) instabilities we need only evaluate the asymptotic time dependence of the response for our time-space delta-function source. This is most conveniently done by deforming the path of integration of Eq. 4 in the ω-plane as far as possible into the upper half ω-plane. The asymptotic time dependence of the response, $\Psi(t, z)$, is then determined by the lowest singularity of the function $F(\omega, z)$ in the ω-plane. If this lowest singularity occurs for $\omega_i < 0$, the system exhibits an absolute instability, with a growth rate in time given by that particular value of $\omega_i$. If, on the other hand, this lowest singularity occurs for $\omega_i > 0$, the system does not exhibit an absolute instability, and a steady state in time may be reached.

The investigation of the analytic properties of $F(\omega, z)$ is most conveniently illustrated by considering the motion of a single frequency from the contour L as shown in Fig. X-17a. As the frequency changes from $\omega_L$ to $\omega_R$, the k-plane singularities of

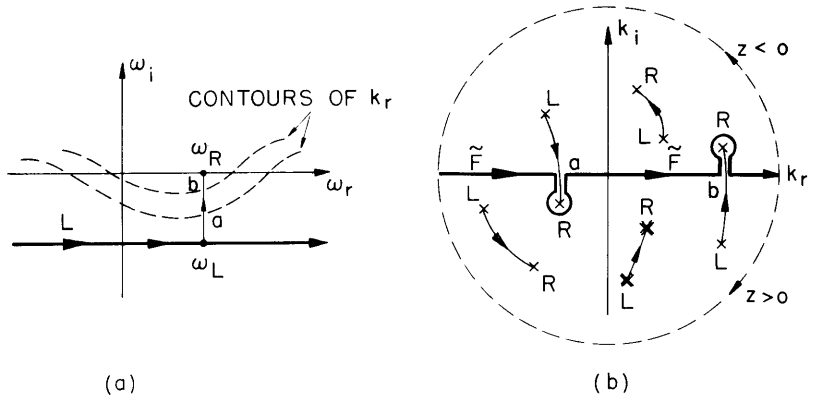


Fig. X-17. As the frequency changes along the path $\omega_L$ to $\omega_R$ (a), the singularities of $G(\omega, k)$ describe the loci shown in (b).

$G(\omega, k)$, for the particular values of $\omega$, describe the loci shown in Fig. X-17b. It is then clear from Eqs. 3, 5, and 6 that $F(\omega, z)$ will be discontinuous unless the contour F is deformed into the contour $\tilde{F}$ so as to include (or exclude) any poles that cross the real k axis, that is, the contours of the real k axis in the $\omega$-plane (Fig. X-17a) represent branch lines of the function $F(\omega, z)$ as defined by the integration in Eq. 3. The contour L may be deformed past these branch lines without altering the integration in Eq. 4 if $F(\omega, z)$ is properly analytically continued by evaluation along the contour $\tilde{F}$. This procedure now can be extended, in principle, to all frequencies on the contour L.

The singularities of $F(\omega, z)$ are discovered in this process of sweeping the complex $\omega$-plane from the contour L up. These singularities will occur for frequencies at which two or more poles of $G(\omega, k)$ merge <u>through</u> the contour $\tilde{F}$ to form a higher order pole,

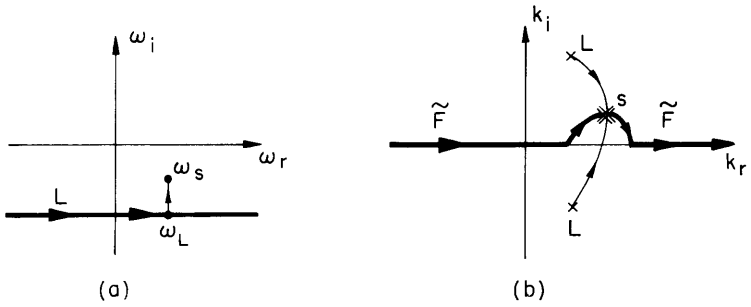


Fig. X-18. Appearance of an absolute instability. At the frequency $\omega_s$: (a) the two simple poles of $G(\omega, k)$ merge through the contour $\tilde{F}$ to form a double-order pole in the k-plane; (b) $\omega_s$ is then a branch pole of $F(\omega, z)$.

since then the integration must pass between the merging poles. The simplest situation of such a merging of two simple poles is illustrated in Fig. X-18. In the vicinity of the merger of the poles, we have

$$(k-k_s)^2 \sim (\omega-\omega_s), \tag{7}$$

and the evaluation (Eqs. 5 and 6) gives

$$F(\omega, z) \sim \frac{1}{(\omega-\omega_s)^{1/2}}, \tag{8}$$

which shows that $\omega_s$ is a branch pole of $F(\omega, z)$. If for the moment we consider this to be the lowest singularity of $F(\omega, z)$ in the $\omega$-plane, then the asymptotic time dependence of the response can be evaluated along the contour L shown in Fig. X-19, and the

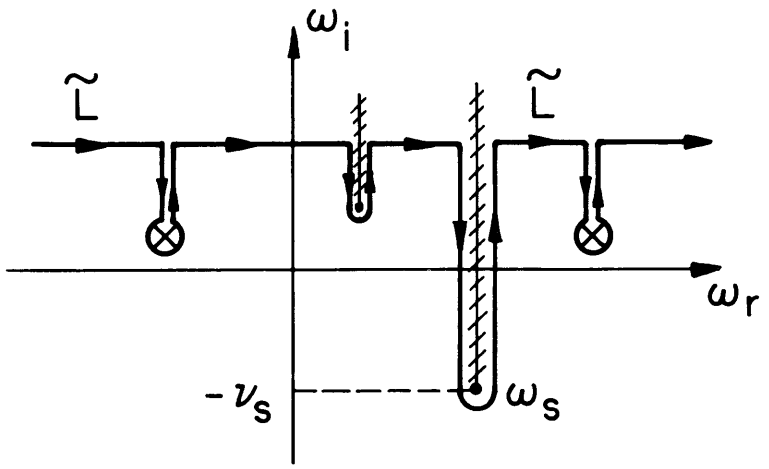


Fig. X-19. Contour L for the asymptotic evaluation of Eq. 4. As the contour is moved up toward $\omega_i \to \infty$, the dominant contribution to the response for $t \to \infty$ comes from the integration along the branch line ending at $\omega_s = \omega_{rs} - j\nu_s$.

dominant contribution will come from the integration along the branch line ending at $\omega_s$. For the branch pole of Eq. 8, for $t \to \infty$ we find

$$\Psi(t, z) \to \frac{e^{\nu_s t}}{t^{1/2}} e^{j(\omega_{rs} t - k_s z)}, \tag{9}$$

and we conclude that the system exhibits an absolute instability. We note that the condition of a double root of k for some $\omega = \omega_s$ is the same as the condition that $\omega(k)$ have a saddle point at $\omega = \omega_s$. If this saddle point is to lead to a true singularity of $F(\omega, z)$ (and hence to an absolute instability), it is crucial that this saddle point result from two k-plane poles that merge <u>through</u> the contour $\tilde{F}$.

The merging of poles through the contour $\tilde{F}$ can be readily generalized. Consider the formation of a pole of order p on the contour $\tilde{F}$ at $k = k_s$ and for $\omega = \omega_s$. If, also, the first (n-1) partial derivatives of $D(\omega, k)$ with respect to $\omega$ at $(\omega_s, k_s)$ vanish and $(\partial^n D/\partial\omega^n)_s \neq 0$, then

$$(k-k_s)^p \sim (\omega-\omega_s)^n. \tag{10}$$

For the merging of the poles through the contour $\tilde{F}$, Eqs. 5 and 6 give

$$F(\omega, z) \sim \frac{1}{[\omega-\omega_s]^{(p-1)n/p}}, \tag{11}$$

which may be either poles or branch poles at $\omega_s$. The asymptotic response for $t \to \infty$ is

$$\Psi(t, z) \sim t^{q} e^{\nu_s t}; \qquad q = \frac{(p-1)n}{p} - 1. \tag{12}$$

5. Amplifying, Evanescent, and Propagating Waves

Finally, if $F(\omega, z)$ has no singularities in the lower half of the $\omega$-plane, there are no absolute instabilities, and the uniform system may reach a steady state. In particular, we now may ask for the steady-state asymptotic response of the system at some frequency $\omega = \omega_{rp}$ that is of interest. For this, we consider a source function whose time dependence is a sinusoid of frequency $\omega_{rp}$ that starts at t=0 and is zero for $t<0$. Thus let

$$S(t) \sim e^{j\omega_{rp} t}, \qquad t > 0 \tag{13}$$

$$= 0, \qquad t < 0, \tag{14}$$

and its Laplace transform becomes

$$S(\omega) \sim \frac{1}{j(\omega-\omega_{rp})}. \tag{15}$$

The spatial dependence of the source function may be arbitrary but limited in z; for convenience, we may chose it to be a delta-function.

The asymptotic response of the system for this situation may be obtained (as in sec. 4) by again deforming the contour L of Eq. 4 so that it lies as far up as possible in the upper half of the $\omega$-plane. Since we assume that there are no absolute instabilities, $F(\omega, z)$ has no singularities in the lower half of the $\omega$-plane and the lowest singularity in $F(\omega, z)$ is the pole at $\omega = \omega_{rp}$ belonging to the source function. (Note that we are assuming that the Green's function transform has no singularities on the real $\omega$ axis; if it does, then these will also contribute to the asymptotic response.) Hence the asymptotic time dependence of the response, as evaluated along $\tilde{L}$ in Fig. X-20a, will be sinusoidal at the frequency $\omega_{rp}$ of the source. The space dependence of the response, which is already contained in $F(\omega, z)$, is obtained from the k integration along the proper contour $\tilde{F}$ for $\omega_{rp}$ (as was done in sec. 4; see Fig. X-17). Some of the possible resulting wave solutions are shown in Fig. X-20b. Note that the appearance of a particular wave for $z > 0$ or $z < 0$ is completely determined by the locus of the pole in the k-plane as the frequency is moved from the contour L to the real frequency axis, since in this process the analytic continuation of the function $F(\omega, z)$ determines correctly the position of the k-plane singularities with respect to the contour $\tilde{F}$.

Thus in Fig. X-20b roots 3 and 4, having crossed the $k_r$ axis, are amplifying waves; root 3 is a wave with growth in space for $z > 0$, while root 4 is a wave growing toward $z < 0$. We note that the presence of amplifying waves (convective instabilities) requires that some of the contours of $k_r$ in the $\omega$-plane should have $\omega_i < 0$.

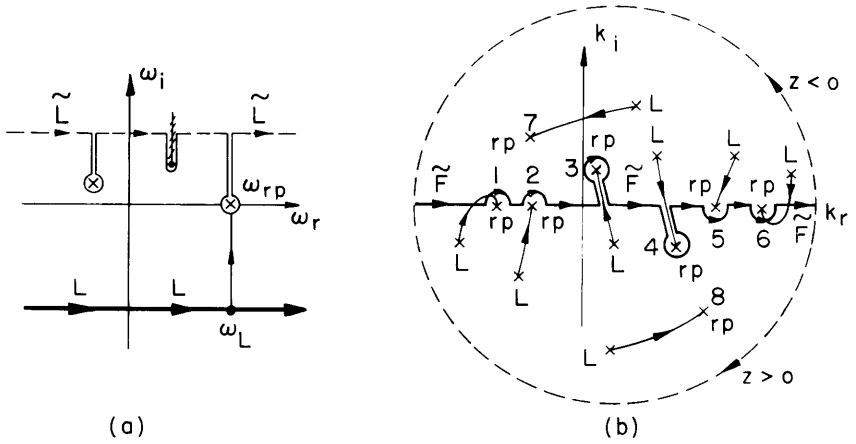


Fig. X-20. System in which there are no absolute instabilities.
(a) Contour L is pushed up to large values of $\omega_i$; the asymptotic time response is determined by $\omega_{rp}$.
(b) The contour $\tilde{F}$ appropriate to $\omega_{rp}$ and the pole loci as the frequency varies from $\omega_L$ to $\omega_{rp}$.

Roots 7 and 8, which have not crossed the $k_r$ axis, are evanescent waves; root 7 is a wave that decays in space for $z < 0$, and root 8 is a wave that decays for $z > 0$.

All of the remaining roots shown in Fig. X-20b are on the real k axis and hence are purely propagating waves. The direction in which they carry the signal is entirely determined by whether these roots appear above or below the F, namely, $\tilde{F}$, contour. Thus waves 1 and 2 will be excited for $z > 0$, and waves 5 and 6 for $z < 0$. Note that the sign of the group velocity, $d\omega/dk$, for these waves will not necessarily give the correct direction in which the signal in each wave will flow. Thus for waves 1 and 6 the group velocity would give the opposite direction to the one determined above, while for waves 2 and 5 it would give the same direction. We therefore note that in systems in which the $k_r$ contours of the dispersion relation in the $\omega$-plane appear for $\omega_i < 0$, the group velocity, in general, will not give the correct direction of signal flow, while our procedure properly determines this direction.

A. Bers, R. J. Briggs

## References

1. R. Q. Twiss, On oscillations in electron streams, Proc. Phys. Soc. (London) B64, 654-665 (1951).

2. L. D. Landau and E. M. Lifshitz, Mechanics of Continuous Media (in Russian) (GITTL, Moscow, 1953), p. 141; also Fluid Mechanics (Pergamon Press, London, 1959), Sec. 29.

3. P. A. Sturrock, Kinematics of growing waves, Phys. Rev. 112, 1488-1503 (1958).

4. O. Buneman, How to distinguish amplifying and evanescent waves, Plasma Physics, edited by J. E. Drummond (McGraw-Hill Book Company, Inc., New York, 1961).

5. Ya. B. Fainberg, V. I. Kurilko, and V. D. Shapiro, Instabilities in the interaction of charged particle beams with plasmas, ZhTF 31, 633-639 (1961); Soviet Phys. – Tech. Phys. 6, 459-463 (1961).

6. R. V. Polovin, Criteria for instability and gain, ZhTF 31, 1220-1230 (1961); Soviet Phys. – Tech. Phys. 6, 889-895 (1962).

## D. INTERACTION OF AN ELECTRON BEAM WITH IONS IN A WARM PLASMA OF FINITE TRANSVERSE DIMENSIONS

In a previous report the dispersion equation for the waves in a waveguide structure filled with a cold electron beam and a hot-electron plasma has been derived, and some computations on the resultant complex propagation constants, $\beta$, for real frequencies $\omega$ are presented.[1] The instability criteria derived by the authors (see Section X-C) has now been applied to the cases discussed previously.[1] It has been found that in all of these cases there is an absolute instability.

In Figs. X-21 and X-22, the loci of (two of) the roots of complex $\beta$ for complex $\omega$ near the saddle point of $\omega(\beta)$ are presented for protons with $\beta_{pb}^2 = p^2$, $n_b/n_p = 10^{-2}$,

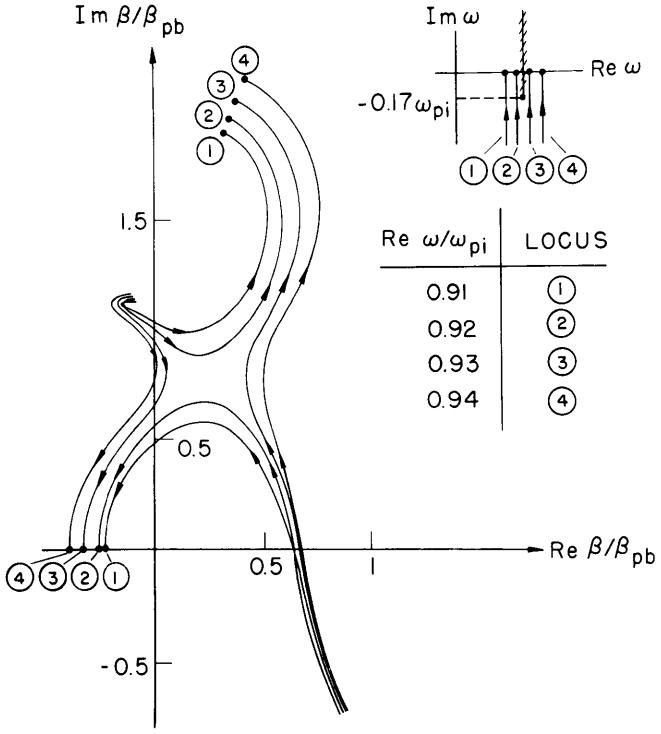


Fig. X-21. Loci of roots of complex $\beta$ for complex $\omega$; $(n_b/n_p)(T_e/2V_o) = 1$.

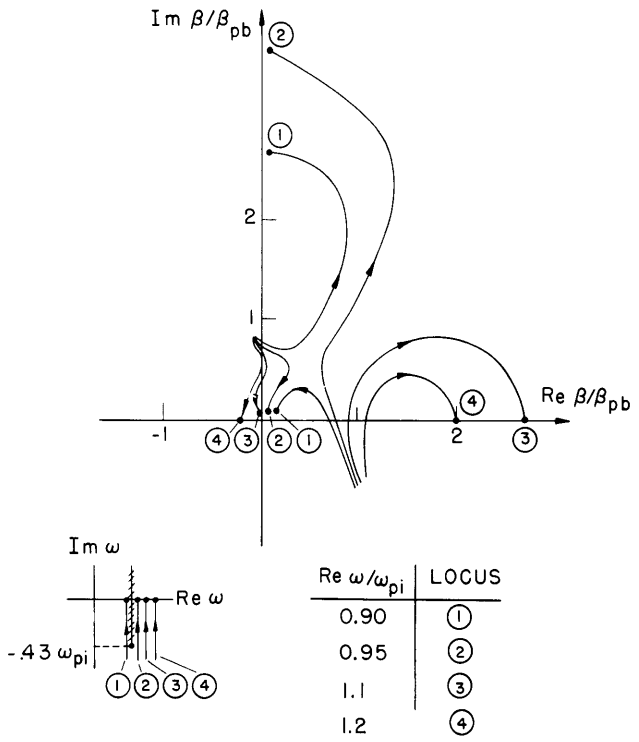


Fig. X-22. Loci of roots of complex $\beta$ for complex $\omega$; $T_e = \infty$.

$\omega_{pi} = 2\omega_{ci}$, and the "temperature parameter" $(n_b/n_p)(T_e/2V_o)$ equal to 1 and $\infty$. (The symbols have been defined by Bers and Briggs.[1]) For these temperature-parameter values there is an absolute instability with growth rates in time of $0.17\omega_{pi}$ and $0.43\omega_{pi}$, respectively.

The presence of the absolute instability has been found to manifest itself in a particular characteristic of complex $\beta$ for real $\omega$ plots, as is indicated in Fig. X-23. For a very weak beam ($\omega_{pb} \ll \omega_{pi}$), the dispersion would have the general shape shown in Fig. X-23a. When an absolute instability is present, the form in Fig. X-23c is obtained. The critical point between the two is indicated in Fig. X-23b; at this critical point there exists a double root of complex $\beta$ for some real $\omega$. Therefore, at the critical point a saddle point of $\omega(\beta)$ is in the process of crossing the real $\omega$ axis. As this saddle point passes into the lower half $\omega$-plane, an absolute instability appears.

The relationship between the parameters which must be satisfied for a double root of complex $\beta$ for real $\omega$ can be derived from the dispersion equation of the system,[1] and is found to be

$$\frac{\omega_{pb}^2}{\omega_{pi}^2} = 1 - \frac{\omega_{ci}^2}{\omega_{pi}^2} - \frac{p^2}{p^2 + \beta_{De}^2 + \beta_{pb}^2} . \tag{1}$$

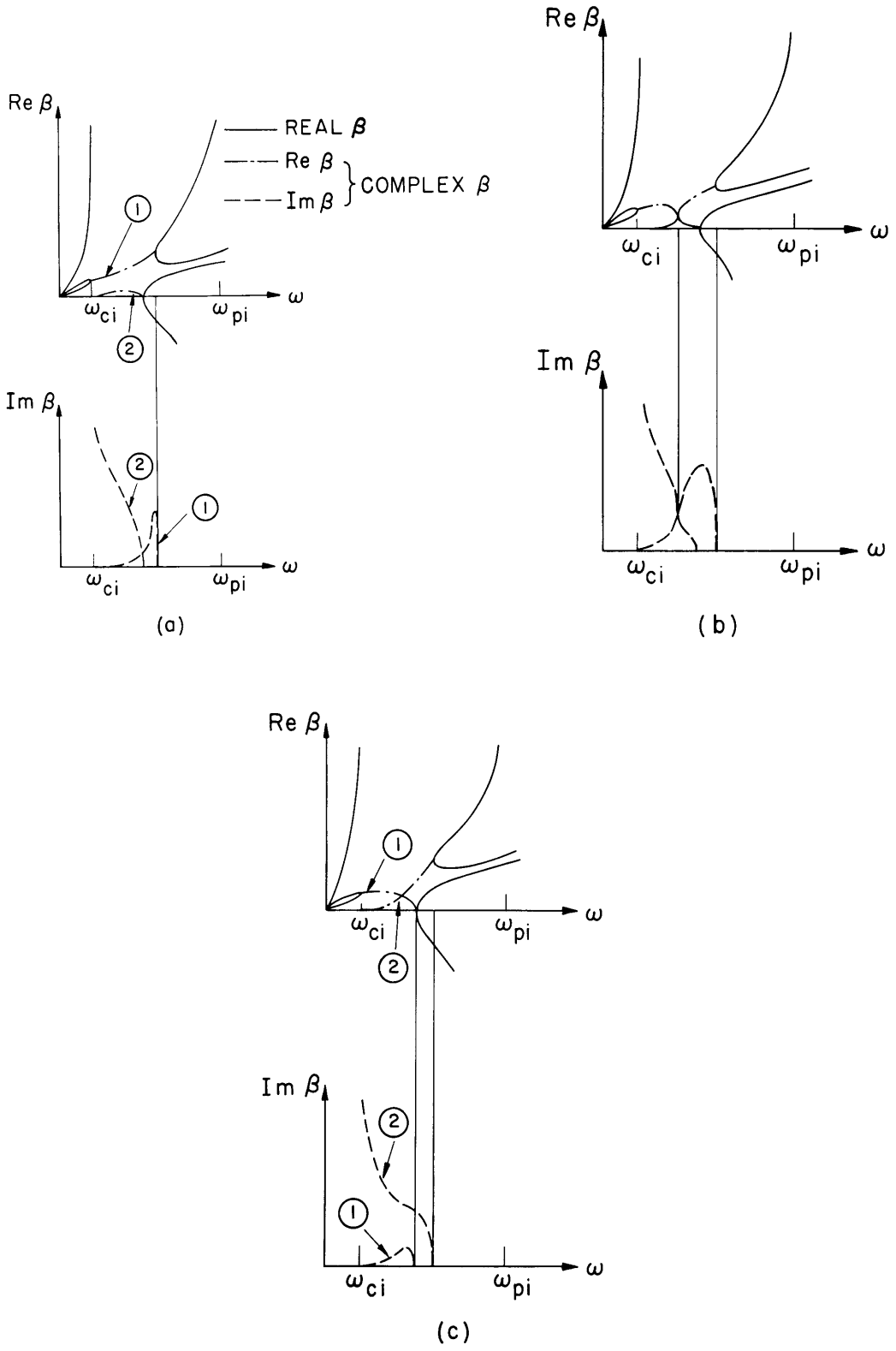


Fig. X-23. Schematic illustration of onset of absolute instability. (a) No absolute instability. (b) Critical point. (c) Absolute instability present.

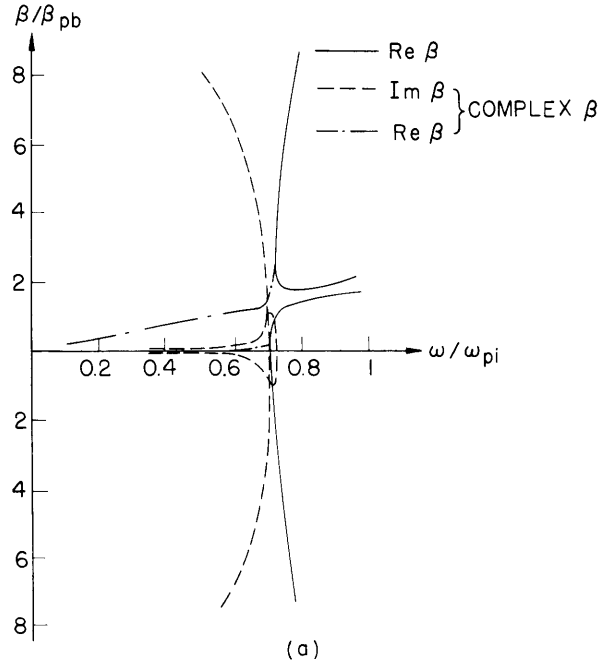


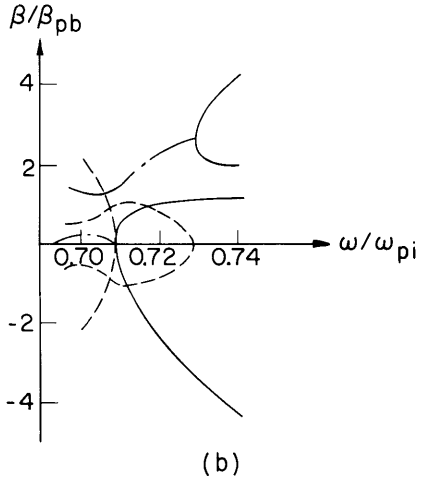


Fig. X-24. (a) Dispersion diagram for $\omega_{pi} = 2\omega_{pb}$.
(b) Detail near $\omega = 0.7\ \omega_{pi}$.

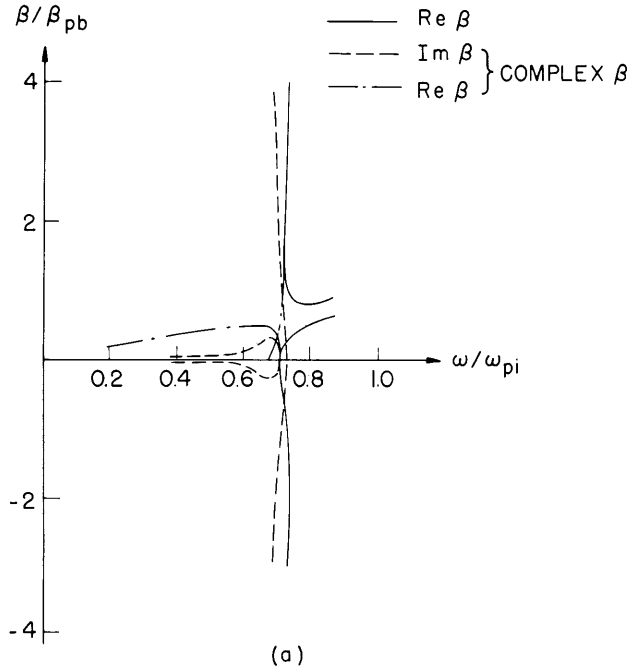


Fig. X-25. (a) Dispersion diagram for $\omega_{pi} = 0.75\ \omega_{pb}$.
(b) Detail near $\omega = 0.7\ \omega_{pi}$.

Some computations that illustrate this transition are presented in Figs. X-24 and X-25. The parameters are $p^2 = 100\,\beta_{pb}^2$, $\beta_{De}^2 = 100\,\beta_{pb}^2$, $\omega_{ci} = 0.05\,\omega_{pi}$, and $\omega_{pi}/\omega_{pb}$ equal to 2 and 0.75. The application of the instability criteria is presented in

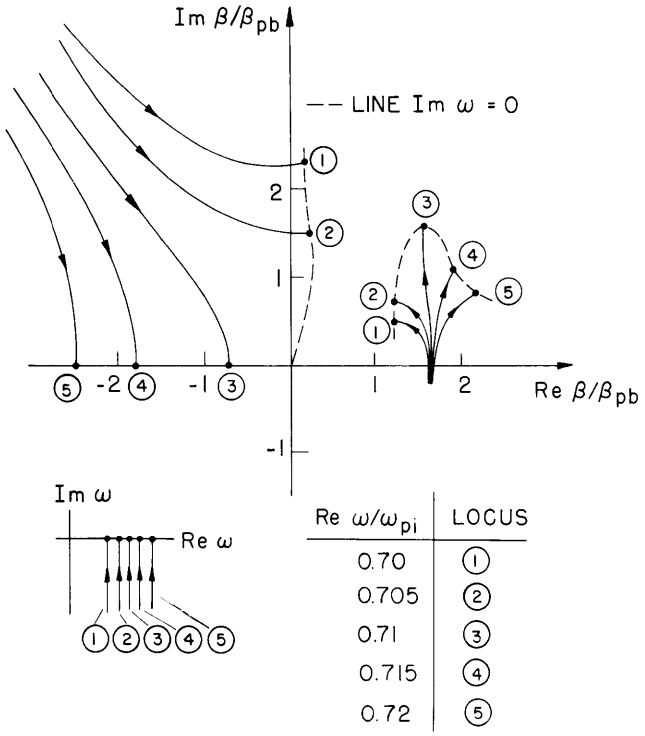


Fig. X-26. Loci of roots of complex $\beta$ for complex $\omega$; $\omega_{pi} = 2\omega_{pb}$

Figs. X-26 and X-27. We see that an absolute instability is obtained in the latter case [$\omega_{pi}/\omega_{pb}$=0.75, Fig. X-27] at a complex frequency $\omega = (0.071 - j0.001)\,\omega_{pi}$.

From the computations that have been performed, two general rules have been found to be valid.

1. An absolute instability arises when

$$\frac{\omega_{pb}^2}{\omega_{pi}^2} > 1 - \frac{\omega_{ci}^2}{\omega_{pi}^2} - \frac{p^2}{p^2 + \beta_{De}^2 + \beta_{pb}^2}. \tag{2}$$

2. Infinite amplification at $\omega = \omega_{pi}$ arises when

$$\beta_{pb}^2 + p^2 \frac{\omega_{ci}^2}{\omega_{pi}^2 - \omega_{ci}^2} > \beta_{De}^2. \tag{3}$$

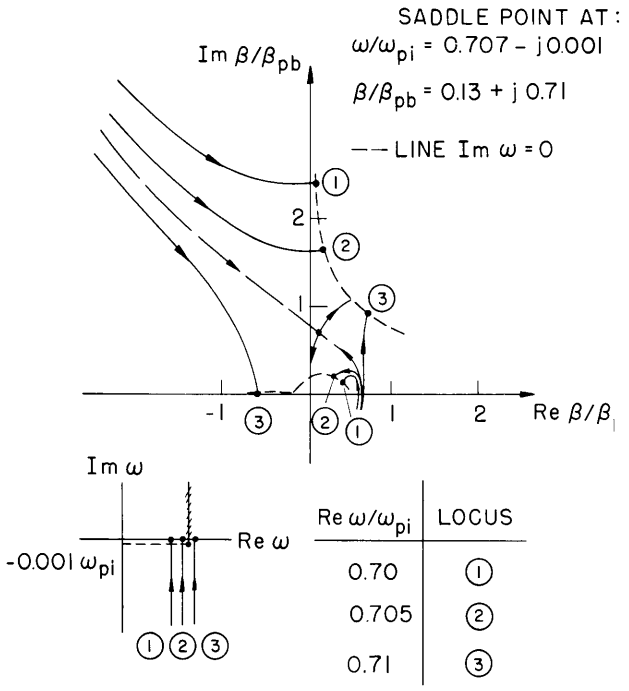


Fig. X-27. Loci of roots of complex $\beta$ for complex $\omega$; $\omega_{pi} = 0.75\ \omega_{pb}$.

These two conditions are independent of each other. In all of this analysis, it was assumed that $V_o \ll V_{Te}$. The extension of these results to cases in which $V_{Te}$ is comparable to $V_o$ is under consideration.

R. J. Briggs, A. Bers

References

1. R. J. Briggs and A. Bers, Interaction of an electron beam with ions in a warm plasma of finite transverse dimensions, Quarterly Progress Report No. 70, Research Laboratory of Electronics, M.I.T., July 15, 1963, pp. 129-133.

## E. FUSION REACTOR BLANKET EXPERIMENT: NEUTRON-ENERGY SPECTRUM FROM A TRITIUM-GAS TARGET

The threshold detectors that will be used to determine the neutron-energy spectrum in fusion reactor blanket mock-ups[1] will be calibrated by irradiation with the bare tritium-gas target. A derivation of the spectrum of the neutrons from the tritium-gas target is given in this report. A set of Fortran II programs has been written to perform the calculations.

### 1. Point-Source Calculation

When deuterons of energy E' strike a thin tritium target of thickness $d\ell$, it is assumed that their energy loss within the target is negligibly small. The total number

of neutrons produced is $n(E')\,d\ell$.

$$n(E')\,d\ell = I\,N_t\,\sigma(E')\,d\ell, \tag{1}$$

where I is the deuteron current, $\sigma(E')$ is the cross section for the $H^3(d, n)\,He^4$ reaction (DT reaction), $N_t$ is the tritium number density, and $d\ell$ is the thickness of the target. For bombarding energies $E' < 0.4$ Mev, the DT reaction is isotropic in the center-of-mass (c.m.) coordinate system[2]; hence the fraction of neutrons that are emitted at an angle $\theta^* = \cos^{-1} x^*$ in c.m. coordinates within the solid angle $d\Omega^* = \sin\theta^*\,d\theta^*\,d\phi^*$ is just $d\Omega^*/4\pi$. The calculations are simplified if, instead of using $\theta^*$ as the independent variable, we use the direction cosine $x^*$; then $d\Omega^* = -dx^*\,d\phi^*$. The fraction in the solid angle $d\Omega = \sin\theta\,d\theta\,d\phi = -dx\,d\phi$ in the laboratory coordinate system at angle $\theta$ is found by using the appropriate transformation

$$d\Omega^* = -dx^*\,d\phi^* = -j(E', x)\,dx\,d\phi = j(E', x)\,d\Omega. \tag{2}$$

The fraction of the neutrons that pass through an elemental area $dA = r^2\,d\Omega$ at the point $(r, \cos^{-1} x, \phi)$ is then $j(E', x)\,dA/4\pi r^2$. Hence the number of neutrons that pass through this point, which are produced by the deuterons of energy $E'$ in the target of thickness $d\ell$, is $\phi_\ell(E', x, r)\,d\ell\,dA$:

$$\phi_\ell(E', x, r)\,d\ell\,dA = I\,N_t\,\sigma(E')\,\frac{j(E', x)}{4\pi r^2}\,d\ell\,dA. \tag{3}$$

All of these neutrons have an energy $E = f(E', x)$. A derivation of $f(E', x)$ and $j(E', x)$ has been given.[3] These functions, as well as the solution of the equation $E = f(E', x)$ for $E'$ ($E' = g\{E, x\}$), are presented in Table X-1.

In a gas target the deuterons slow down (mainly by elastic collisions with the electrons in the gas) at a rate given by

$$dE'/d\ell = -N_t\tau(E'), \tag{4}$$

where $\tau(E')$ is the stopping cross section for deuterons in tritium gas (in Mev-barns). To account for the moderation of the deuterons, we split the gas target into many small slabs of thickness $d\ell$, which are such that the deuteron energy within these slabs may be considered constant. We shall consider a slab in which the deuterons have reached energy $E'$ ($< E'_{max}$, the energy of the deuterons incident on the gas target). We use Eq. 4 to convert $d\ell$ to the appropriate energy width and find that the flux of neutrons through the point $(r, \cos^{-1} x, \phi)$, produced by deuterons between energies $E'$ and $E' + dE'$, is

$$\phi'(E', x, r)\,dE' = I\,\frac{\sigma(E')}{\tau(E')}\,\frac{j(E', x)}{4\pi r^2}\,dE'. \tag{5}$$

To obtain $\phi(E, x, r)$, the flux of neutrons per unit neutron-energy width at the point

Table X-1. Energy-angle relationships for the nuclear reaction $M_2(M_1, M_3)M_4$. Here, E' is the energy of the inc nuclide $M_1$ in laboratory coordinates; E is the laboratory energy of $M_3$ after the reaction; x is the c of the angle between the paths of $M_3$ and $M_1$ in laboratory coordinates; $x^*$ is the same cosine in cente mass coordinates; $m_i$ is the mass of the $i^{th}$ nuclide $M_i$; and $Q = \{(m_1+m_2)-(m_3+m_4)\}c^2$, where c velocity of light. The derivation of these equations has been given elsewhere.[3]

| Functions | Equations | Restrictions |
|---|---|---|
| $f(E', x) = E$ | $\sqrt{E} = \frac{\sqrt{m_1 m_3}}{m_3 + m_4}\left[x\sqrt{E'} \pm \left[x^2E' + (m_4/m_3+1)\{(m_4/m_1)(Q+E')-E'\}\right]^{1/2}\right]$ | $\sqrt{E}$ Real<br>$\sqrt{E} \geq 0$<br>(See Note A) |
| | $x^* = -(1-x^2)\{a(E')\} \pm \left[1-(1-x^2)\{a(E')\}^2\right]^{1/2}$ | $x^*$ Real |
| | $a(E') = \left[(m_1 m_3/m_2 m_4)/\{1+(Q/E')(m_1/m_2+1)\}\right]^{1/2}$ | $\lvert x^* \rvert \leq 1$ |
| $j(E', x) = \partial x^*/\partial x$ | $\partial x^*/\partial x = 2x\, a(E') \pm \left[1-(1-x^2)\{a(E')\}^2\right]^{1/2}\left[1 + \frac{x^2\{a(E')\}^2}{1-(1-x^2)\{a(E')\}^2}\right]$ | (See Note A) |
| $g(E, x) = E'$ | $\sqrt{E'} = \frac{\sqrt{m_1 m_3}}{m_4 - m_1}\left[-x\sqrt{E} \pm \left[x^2E + (m_4/m_1-1)\{E-(m_4/m_3)(Q-E)\}\right]^{1/2}\right]$ | $\sqrt{E'}$ Real<br>$\sqrt{E'} \geq 0$<br>(See Note B) |

Note A: Where ± occurs, only the plus sign may be used if $Q > 0$ for restrictions to be satisfied; for $Q < 0$, both are sometimes possible; that is, the function is double-valued.

Note B: Reverse of Note A; only the plus sign may be used for $Q < 0$, but the function is sometimes double-v when $Q > 0$.

$(r, \cos^{-1} x, \phi)$, it is only necessary to change the energy width in Eq. 5 from dE' to dE:

$$dE' = \frac{dE}{(dE/dE')_{x=\text{const.}}} , \tag{6}$$

where

$$(dE/dE')_{x=\text{const.}} = \partial f(E', x)/\partial E' \qquad \text{(point source)} \tag{7}$$

for $r \gg \ell_o$, the thickness of the gas target. By substituting Eqs. 6 and 7 for dE' in Eq. 5, the desired expression for $\phi(E, x, r)$ is found to be

$$\phi(E, x, r) = I \frac{\sigma(E')}{\tau(E')} \frac{j(E', x)}{4\pi r^2} \{\partial f(E', x)/\partial E'\}^{-1} , \tag{8}$$

where $E' = g(E, x)$. Only the magnitudes of $j(E', x)$ and $\partial f(E', x)/\partial E'$ are used, since only the magnitudes of $(d\Omega^*/d\Omega)_{E'=\text{const.}}$ and $(dE/dE')_{x=\text{const.}}$ are of interest. A sample set of spectra at various angles, calculated from Eq. 8, is plotted in Fig. X-28 as $r^2\phi(E, x, r)$ vs E.

## 2. Numerical Problems

The function $f(E', x) = E$ for a given value of x has the general shape shown in Fig. X-28. From the figure it can be seen that if $E'_{max} > E'_m$ and $E'_{min} < E'_m$, where $E'_{min}$ is the energy at which unreacted deuterons leave the target, and

$$\partial f(E', x)/\partial E' = 0 \qquad (E'=E'_m), \tag{9}$$

there may be two deuteron energies E' that can produce neutrons of energy E $(E_{min} \leq E \leq E_1 = f(E'_m, x))$. The fluxes resulting from each of these E' are then added.

Since $\partial f/\partial E'$ appears in the denominator of Eq. 8, $\phi(E_{min}, x, r)$ is singular if $E_{min} = f(E'_m, x)$. The singularity may be formally avoided by adding a small increment to $E_{min}$. Since the zero of $\partial f/\partial E'$ is calculated from the difference of numbers that are accurate to, at most, one part in $10^4$, there will be large round-off errors in $\phi(E, x, r)$ in regions near $\partial f/\partial E' = 0$. If $\phi(E, x, r)$ is being used in an integration – to find the average of a cross section $\sigma'(E)$, for instance, for which the detailed shape of the neutron-energy spectrum is not desired – it is better to use Eq. 5, integrate over deuteron energy, and use $\sigma'\{f(E', x)\}$ in the integral. Then the problem of singularities does not arise.

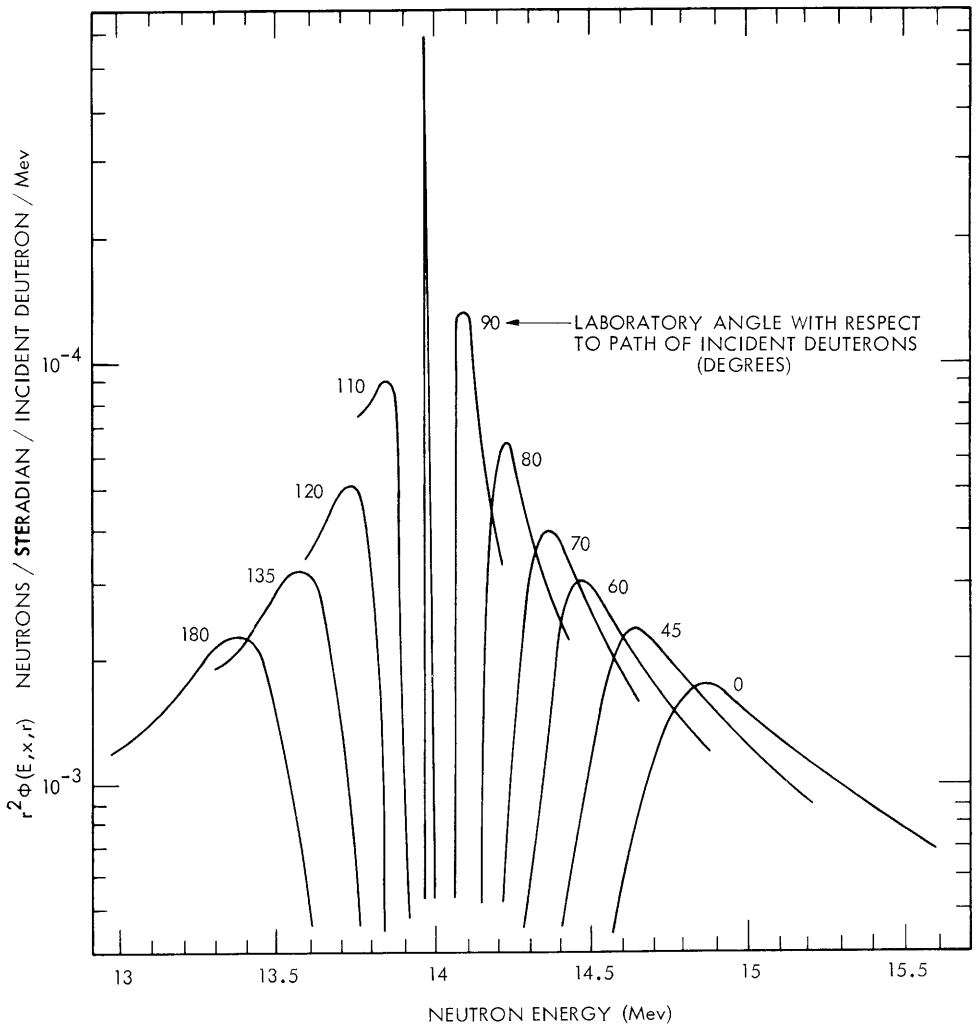


Fig. X-28. Point-source calculation of neutron-energy spectrum from gas target. Target length, 3.175 cm; target pressure, 0.42 atm of tritium; deuterons enter gas at 0.4 Mev and leave at 0.04 Mev. Note that the spectrum has the general shape of the DT cross section, distorted by division by $(dE/dE')_{x=const.}$, a value that is positive at 0°, passes through zero at ~100°, and then becomes negative. Note that for 0° the spectrum immediately drops to zero at 15.6 Mev. The spectrum drops to zero at 15.25 Mev for 45°, etc.

3. Finite-Source Calculation

If the distance r of the point of observation P from the target is of the same order as the thickness of the target $\ell_o$ (see Fig. X-29), the calculation of $\phi(E, x, r)$ is more

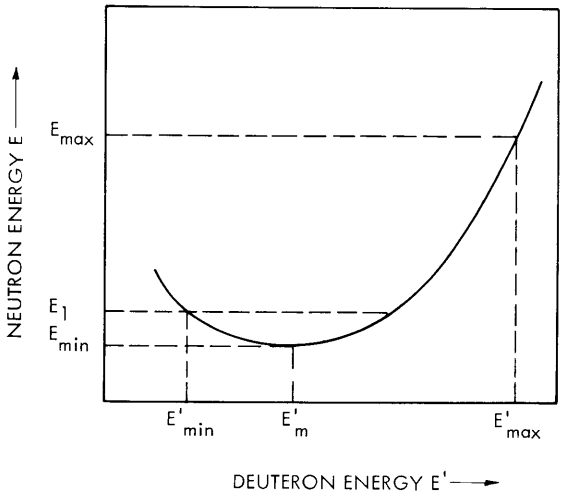


Fig. X-29. Schematic curve of $E = f(E', x)$ for a constant value of x.

complicated than is outlined in section 1.

As the deuterons slow to energy E', they travel a distance $\ell = \ell(E')$:

$$\ell(E') = \int_{E'}^{E'_{max}} dE'/N_t\tau(E'). \tag{10}$$

As can be seen from Fig. X-30, the neutrons produced by the deuterons that pass through the point P now travel a distance R, given by

$$R^2 = r^2 + \ell^2 - 2rx\ell. \tag{11}$$

The cosine of the angle between R and the deuteron path is now not x by y, where

$$y = (r - \ell)/R. \tag{12}$$

The energy of the neutrons is $E = f(E', y)$ and the ratio of the solid angles in c.m. and laboratory coordinates is $j(E', y)$. Furthermore, $(dE/dE')_{x=const.}$ is no longer simply $\partial f/\partial E'$ but

$$(dE/dE')_{x=const.} = \frac{\partial f(E', y)}{\partial E'} + \frac{\partial f(E', y)}{\partial y}\frac{dy}{d\ell}\frac{d\ell}{dE'} \qquad \text{(finite source)}. \tag{13}$$

We find $d\ell/dE'$ from Eq. 4; $dy/d\ell$ can be found by differentiating Eq. 11.

$$dy/d\ell = (y^2-1)/R. \tag{14}$$

The expression for the neutron-energy spectrum $\phi(E, x, r)$ for a finite source is found from Eq. 8 by replacing x with y, r with R, and $\partial f/\partial E'$ with Eq. 12:

$$\phi(E, x, r) = I \frac{\sigma(E')}{\tau(E')} \frac{j(E', y)}{4\pi R^2} \left\{ \frac{\partial f(E', y)}{\partial E'} - \frac{\partial f(E', y)}{\partial y} \frac{(y^2-1)}{R\, N_t \tau(E')} \right\}^{-1} \quad \text{(finite source).} \tag{15}$$

Here, $dy/d\ell$ and $d\ell/dE'$ have been replaced with the right-hand side of Eqs. 4 and 14. It is no longer possible to find the deuteron energy E' analytically from the neutron energy E and the coordinates of the point of observation $(r, \cos^{-1} x, \phi)$; a numerical

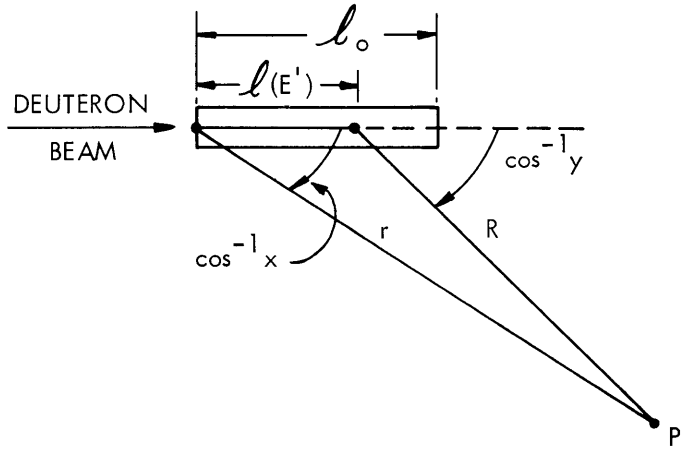


Fig. X-30. Schematic diagram of a gas target for finite-source calculation.

approach must be used.

A sample calculation of the neutron-energy spectrum for $\cos^{-1} x = 70°$ is shown in Fig. X-30 for various radii. Notice in Eq. 15 that as r becomes large $y \rightarrow x$, $R \longrightarrow r$, and the second term in braces becomes much smaller than the first; thus Eq. 15 approaches Eq. 8 for the point source. This is shown in Fig. X-31, in which the results of the finite-source calculation merge with those of the point-source calculation as r increases. The spectrum broadens as r decreases, since the neutrons that pass through the point of observation can come from a wider range of angles with the deuteron path. The continued increase of the spectrum as E approaches 13.93 for r = 5 cm is caused by the fact that in this case the term in braces in Eq. 15 approaches zero. The problems of singularities in $\phi(E, x, r)$ for the finite-source calculation are similar

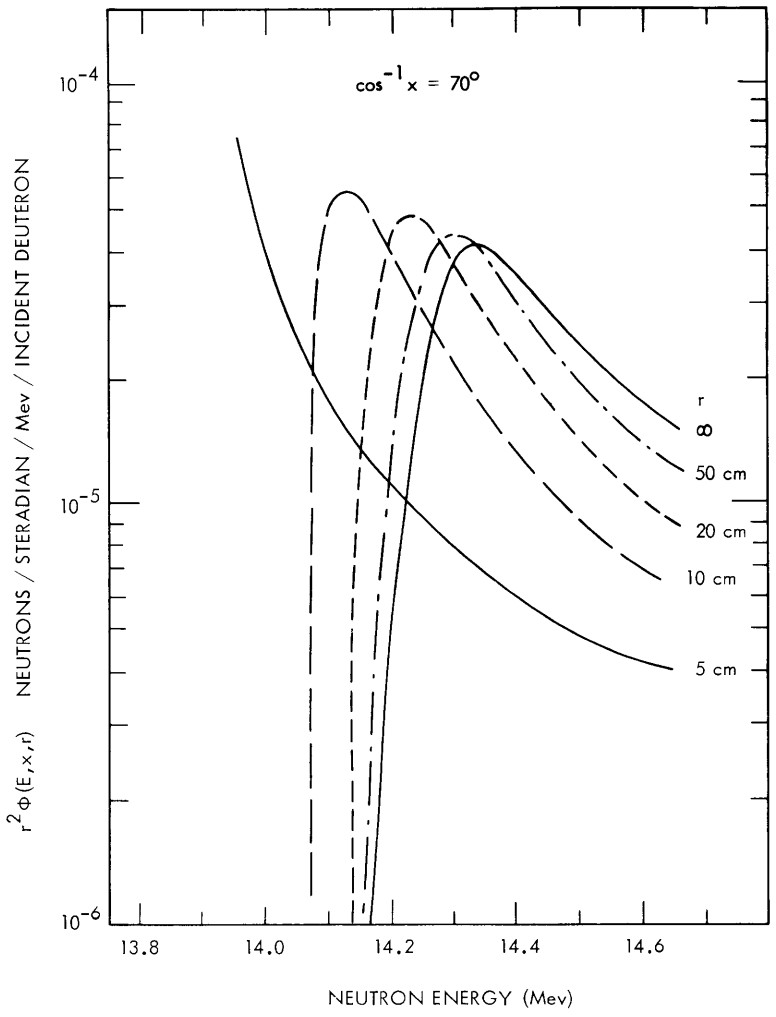


Fig. X-31. Finite-source calculation of neutron-energy spectrum from tritium-gas target. Target is 3.175 cm thick and contains 0.41 atm of tritium. Maximum deuteron energy, 0.4 Mev; minimum deuteron energy, 0.034 Mev. r is the distance of the point of observation from the target window at which the deuterons enter the target at 0.4 Mev ($r = \infty$ refers to the point-source calculation shown in Fig. X-28). The angle between r and the deuteron path is 70°.

to those discussed for the point-source calculation in section 2.

4. Generalizations

a. Deuteron Depletion

In Eqs. 5, 8, and 15, it is implicitly assumed that the deuteron current is not reduced in passage through the target. A correction for this depletion can be made by multiplying the right-hand side of each of these equations by the term

$$\exp\left\{-\int_{E'}^{E'_{max}} dz\ \sigma(z)/\tau(z)\right\},$$

but this correction is unnecessary, since less than 1 deuteron in 1000 undergoes a DT reaction as it transverses the target.

b. Solid Tritium Target

If the tritium, instead of being in the gaseous phase, is absorbed in a solid, Eq. 4 would have to be replaced by

$$dE'/d\ell = -N_t\tau(E') - N_s\tau_s(E'), \tag{16}$$

where $\tau_s(E')$ is the stopping cross section, and $N_s$ is the number density of the solid material. Then $\tau(E')$ on the right-hand side of Eqs. 5, 8, and 15 would have to be replaced by $\tau(E') + (N_s/N_t)\tau_s(E')$. Since in most solid tritium targets $N_s/N_t \geq 1$, and $\tau_s(E')$ is roughly proportional to $\sqrt{Z_s}$, where $Z_s$ is the atomic number of the solid material, the reason for the increased efficiency of the gas target (in neutrons per deuteron) becomes apparent. The increased slowing-down rate of the deuterons in the solid target decreases their chance of undergoing a DT reaction.

c. Other Reactions

Obviously, the expressions above can be applied to any charged-particle reaction by using the appropriate values of the parameters involved. If the Q-value of the reaction is negative, a singularity in $\phi(E, x, r)$ cannot occur. Then, however, cases do arise for which neutrons of two distinct energies can be produced at the same angle $\cos^{-1} x$ by a given deuteron energy $E'$ in the laboratory coordinate system, since with a negative Q-value the functions $f(E', x)$ and $j(E', x)$ may be double-valued.

P. S. Spangler

References

1. P. S. Spangler, Fusion reactor blanket experiment, Quarterly Progress Report No. 69, Research Laboratory of Electronics, M.I.T., April 15, 1963, pp. 81-88.

2. N. Jarmie and J. D. Seagrave (eds.), Charged Particle Cross Sections, AEC Report No. LA-2014, Los Alamos Scientific Laboratory, University of California, Los Alamos, New Mexico, March 1956, p. 41.

3. R. D. Evans, The Atomic Nucleus (McGraw-Hill Book Company, New York, 1955), pp. 408-421; 828-836.